PHOTONICS Research

Improvement of terahertz beam modulation efficiency for baseless all-dielectric coded gratings

Jie Jiang,[1,2] Bo Fang,[3] Chenxia Li,[1,2] Zhi Hong,[2] and Xufeng Jing[1,2,*]

[1]Institute of Optoelectronic Technology, China Jiliang University, Hangzhou 310018, China
[2]Centre for THz Research, China Jiliang University, Hangzhou 310018, China
[3]College of Metrology & Measurement Engineering, China Jiliang University, Hangzhou 310018, China
*Corresponding author: jingxufeng@cjlu.edu.cn

Received 17 May 2023; revised 27 July 2023; accepted 3 August 2023; posted 3 August 2023 (Doc. ID 495532); published 28 September 2023

Optical metasurfaces are two-dimensional ultrathin devices based on single-layer or multilayer arrays of subwavelength nanostructures. They can achieve precise control of phase, amplitude, and polarization on the subwavelength scale. In this paper, a substrate-free all-silicon coded grating is designed, which can realize the phase control of the outgoing beam after the *y*-polarized plane wave is vertically incident on the metasurface at 0.1 THz. Through a single-layer silicon nanoarray structure, a low-reflection anomalous transmission metasurface is realized, and a variety of different beam deflectors are designed based on these encoded gratings. We propose a coded grating addition principle, which adds and subtracts two traditional coded grating sequences to obtain a new coded grating sequence. The encoded supergrating can flexibly control the scattering angle, and the designed substrate-free all-silicon encoded grating can achieve a deflection angle of 48.59°. In order to verify the principle of coded grating addition, we experimented with cascade operation of two coded sequence gratings to obtain the flexible control of the terahertz beam of the composite supergrating. The principle of grating addition provides a new degree of freedom for the flexible regulation of the terahertz wavefront. At the same time, this method can be extended to the optical band or microwave band, opening up new ways for electromagnetic wave manipulation and beam scanning.

https://doi.org/10.1364/PRJ.495532

1. INTRODUCTION

The metasurface is a structured array developed in recent years to adjust the wavefront of electromagnetic waves, which has attracted extensive attention in the field of micro-nanophotonics [1,2]. Such superstructured surfaces mainly control the electromagnetic field through the accumulation of phase mutations in single or multilayer scatterers [3]. A metasurface is a two-dimensional metamaterial whose thickness is much smaller than the wavelength of the incident light [1] and can adjust and control the basic characteristics of the incident light such as phase and amplitude [4]. The fabrication of three-dimensional metamaterial optical devices requires delicate fabrication techniques, while two-dimensional metasurfaces contain only one or a few layers of planar nanostructure arrays, thus greatly reducing the loss of light transmission [5,6]. Generally speaking, researchers can realize metasurface functional devices such as biological detection [7–9], holographic imaging [10], vortex beam generation [11], and stealth [12] through resonance phase, waveguide transmission phase, and Pancharatnam–Berry phase [13].

Electromagnetic wave phase control is one of the most widely used research directions on metasurfaces [1,2]. The metasurface is composed of many meta-atoms, so we can control the phase of each meta-atom through the phase function [3], so as to design the properties of the metasurface we want. In recent years, dielectric nanostructures based on low loss [14] and high refractive index [15–17] have aroused great interest among researchers, especially the performance of semiconductor metasurfaces [18]. Dielectric nanostructures overcome the problem of loss in metallic metasurfaces, and they possess both electric and magnetic dipoles upon excitation [19]. Cui *et al.* [20] proposed a seven-layer (from top to bottom: quartz, complementary split ring resonator, polyimide, liquid crystal, polyimide, metal grinding, and silicon substrate) structure, using reflective-like [21] grating metasurfaces for frequency-steered beam steering. Based on the theoretical prediction of the grating principle [22], when the frequency of the vertically incident terahertz wave varies between 0.87 and 1.02 THz, the metasurface grating can steer the deflected beam from 59.5° to 47.3°. To generate arbitrary optical vortices [12], Wang *et al.* designed and demonstrated a chip-scale device based on an all-dielectric [23] two-dimensional polarization-independent metasurface [24,25] grating [26]. Based on the principles of

multi-beam interference and nanofabrication techniques, the designed devices allow high efficiency [27–29] while also being able to generate on-chip multi-channel beams with different angular momentums [30–32]. In order to improve the diffraction efficiency, Pottier *et al.* [33] fabricated a planar concave integrated optical diffraction grating using a grating distributed Bragg reflector based on a dielectric material [34]. They combined the Bragg conditions that produce high reflection [35] with the grating diffraction conditions that provide wavelength diffusion, constructed a single-order diffraction grating using elliptical sections [36,37], and finally made the diffraction efficiency of the single-order grating reach 99%. In addition, all-dielectric metalenses [38] have aroused great interest among researchers due to their advantages of low loss [39], high efficiency [40], and low cost [4], especially all-dielectric metalenses based on silicon materials [41]. Metalenses [42] can be combined with large-scale semiconductor fabrication techniques for large-scale industrial production [43].

Most current grating metasurface designs are based on two or more different materials [44,45] to manipulate electromagnetic waves to achieve different functions [46]. Most metasurface photonic devices are designed and fabricated on thicker substrate materials [47–51]. The presence of the base structure leads to a decrease in device efficiency, especially for transmissive metasurface devices [52,53]. In this paper, we propose a substrate-free all-dielectric silicon grating structure. At the frequency of 0.1 THz, the subwavelength coding grating unit can achieve 2π phase mutation and has high transmission efficiency. Based on the classical grating equation, a new coded hypergrating is obtained by adding and subtracting two different sequences of coded hypergratings. Through the four-bit operation, the maximum deflection angle of the grating is 48.59°. We encode this baseless grating, and each coding unit can be moved and arranged randomly, which further improves the design flexibility of traditional grating. It is worth noting that, based on the traditional grating equation, we innovatively propose the addition principle of the coded grating to achieve the multifunctional operation of the traditional grating. In addition to the verification of the basic coded grating beam regulation, we also regulate the metasurface beam deflection of the cascaded silicon grating and realize the superposition of the two coded gratings, which provides a new idea for the design of multifunctional devices. Both simulation and experiment prove the feasibility of substrate-free silicon grating structure for beam regulation.

2. CODED GRATING ADDITION PRINCIPLE

Metagratings combine the resonant scattering properties of the basic unit structure of metasurfaces [54–56] with the intrinsic diffractive properties of gratings [57]. According to the phase transition characteristics of the metasurface [58], we can encode each different unit structure of the metasurface [59]. For example, we can specify a unit structure with a phase difference of 90°, and its digital codes are "0," "1," "2," and "3". For the basic encoding grating of this gradient sequence, its diffraction characteristics conform to the classical grating equation. The traditional gratings we are familiar with are based on the grating equation. The diffraction level and efficiency are optimized and regulated, their design parameters are relatively single, and the functions realized are also relatively traditional. The coding grating addition principle proposed by us can realize the flexible regulation of the unit structure of traditional grating and realize the integration of functions. The coding principle of traditional applications in the process of metasurface design is mainly based on the principle of the phased array antenna, and the scattering characteristics of the coding metasurface are regulated by the Fourier transform characteristics of the near-field and far-field. The principle of coding raster addition proposed here is based on the extension of the classical raster equation, and the two raster equations are coded and added. The coding raster addition principle proposed by us is obviously different from the traditional metasurface coding principle in terms of form and basic physical principles.

The diffraction grating can control the propagation direction of the beam, and the diffraction direction is determined by the grating equation,

$$\sin(\theta_{k'}) - \sin(\theta_{i'}) = k'\frac{\lambda}{\Lambda}. \tag{1}$$

Among them, λ is the wavelength of the incident wave, Λ is the grating period, k' is the diffraction order, $\theta_{i'}$ is the incident angle, and $\theta_{k'}$ is the diffraction angle. When the incident light is vertically incident, the first-order diffraction grating equation simplifies to

$$\sin(\theta_{k'}) = \frac{\lambda}{\Lambda}. \tag{2}$$

Assuming that there are n basic coded super-grating sequences $S_0, S_1, S_2, \ldots, S_n$, then the grating periods are $\Lambda_0, \Lambda_1, \Lambda_2, \ldots, \Lambda_n$, respectively. The first-order diffraction equations of each grating sequence can be expressed as

$$\sin(\theta_0) = \frac{\lambda}{\Lambda_0}, \quad \sin(\theta_1) = \frac{\lambda}{\Lambda_1}, \quad \sin(\theta_2) = \frac{\lambda}{\Lambda_2}, \ldots, \sin(\theta_n) = \frac{\lambda}{\Lambda_n}. \tag{3}$$

Among them, $\theta_0, \theta_1, \theta_2, \ldots, \theta_n$ represent the first-order reflection and diffraction angles of each sequence, respectively. Adding or subtracting these grating sequences in Eq. (3), the new super grating sequence S_m can be obtained as

$$S_{0|\Lambda_0} \pm S_{1|\Lambda_1} \pm S_{2|\Lambda_2} \pm \ldots \pm S_{n|\Lambda_n} = S_m. \tag{4}$$

Each grating sequence of the first-order diffraction equation in Eq. (3) can also be subtracted, and the first-order scattering angle of the new grating sequence S_m can be expressed as

$$\begin{aligned}\sin(\theta_m) &= \sin(\theta_0) \pm \sin(\theta_1) \pm \sin(\theta_2) \pm \ldots \pm \sin(\theta_n) \\ &= \frac{\lambda}{\Lambda_0} \pm \frac{\lambda}{\Lambda_1} \pm \frac{\lambda}{\Lambda_2} \pm \ldots \pm \frac{\lambda}{\Lambda_n}.\end{aligned} \tag{5}$$

If we add and subtract the two grating sequences of S_0 and S_1, Eq. (5) can be simplified, and the corresponding scattering angle can be simplified as

$$\sin(\theta_m) = \sin(\theta_0) \pm \sin(\theta_1) = \frac{\lambda}{\Lambda_0} \pm \frac{\lambda}{\Lambda_1}. \tag{6}$$

3. TRANSMISSIVE SUPERSTRUCTURE CODED GRATING

A. Transmission-Type Unit Particle Design

We designed a transmission-type unit particle using silicon material to achieve 2π phase coverage and high transmittance. Figure 1 shows an encoded metaparticle composed of silicon (the dielectric constant is 11.9, the magnetic permeability is 1, and the losses are negligible) with a unit particle period length P of 1500 μm and a height h of 700 μm.

By changing the width w of the unit particle, the transmission phase of the unit cell can cover the range of 2π. After parameter scanning optimization, four unit structures with a phase difference of 90° can be obtained. When the y-polarized light is perpendicular to the supergrating along the z axis direction, the phase and amplitude characteristics of the cell structure are shown in Fig. 2. At 0.1 THz, the phases of the four units digitally coded as "0," "1," 2," and "3" are −196.96°, −106.94°, −17.43°, and 72.47°, respectively. The transmission coefficients are all greater than 0.82. The geometric parameters of the grating strip width w are 951 μm, 496 μm, 231 μm, and 11 μm, respectively.

B. Transmission-Type Metasurface Basic Sequence

First, the basic sequence as shown in Fig. 3 is designed, encoding is carried out along the x axis direction, and the same encoded particles are used in the y axis direction. The basic sequence codes are $S_1 = 0123\ldots$, $S_2 = 00112233\ldots$, $S_3 = 000111222333\ldots$, all of which are composed of 40 × 30 coded particles. From the above coding composition, it can be seen that the coding periods of the basic sequences S_1, S_2, and S_3 are $\Gamma_1 = 4$ and $P = 6000$ μm; $\Gamma_2 = 8$ and $P = 12{,}000$ μm; and $\Gamma_3 = 12$ and $P = 18{,}000$ μm, respectively. According to the formula $\theta = \arcsin(\lambda/\Gamma)$ of generalized Snell's law [60], the anomalous transmission angles corresponding to the three basic sequences are calculated as $\theta_1 = 30°$, $\theta_2 = 14.47°$, and $\theta_3 = 9.59°$.

The encoding metasurfaces of the above-mentioned transmissive basic sequences S_1, S_2, and S_3 are shown in Fig. 3. In the simulation, the terahertz wave electric field is vertically incident on the encoding metasurface along the y axis direction [61,62], and the boundary conditions in the x, y, and z axis directions are all set to open space [open (add space)].

Figure 3 shows the arrangement of the basic sequence metasurfaces, which correspond to the transmission basic sequences S_1, S_2, and S_3 from top to bottom. According to the simulation calculation results, it can be obtained that $\theta_1 = 30°$, $\theta_2 = 14°$, $\theta_3 = 10°$ (the transmission angle is the included angle with the positive semiaxis of the z axis). These numerical results have little error with the theoretically calculated data. The obvious deflection effect can be seen in both the far-field and the near-field, thus verifying that the designed basic sequence can achieve abnormal transmission.

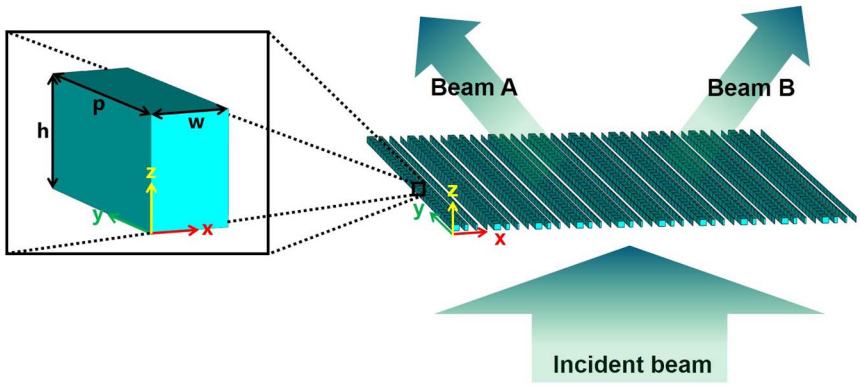

Fig. 1. Three-dimensional schematic diagram and unit diagram of grating.

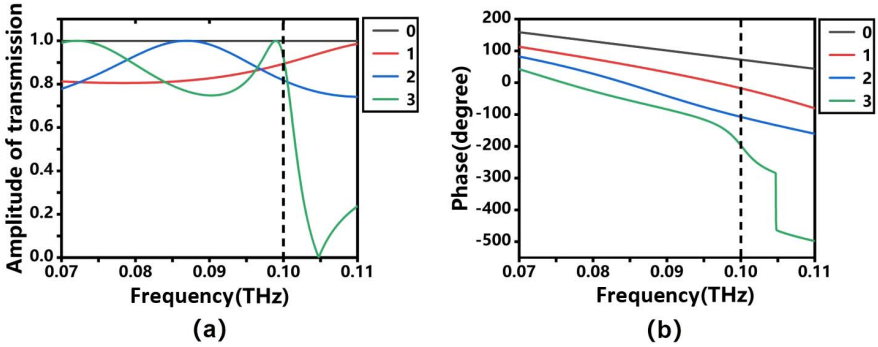

Fig. 2. Structural properties of transmission metamaterials. (a) Transmission amplitude of four kinds of particles. (b) Transmission phase of four kinds of particles.

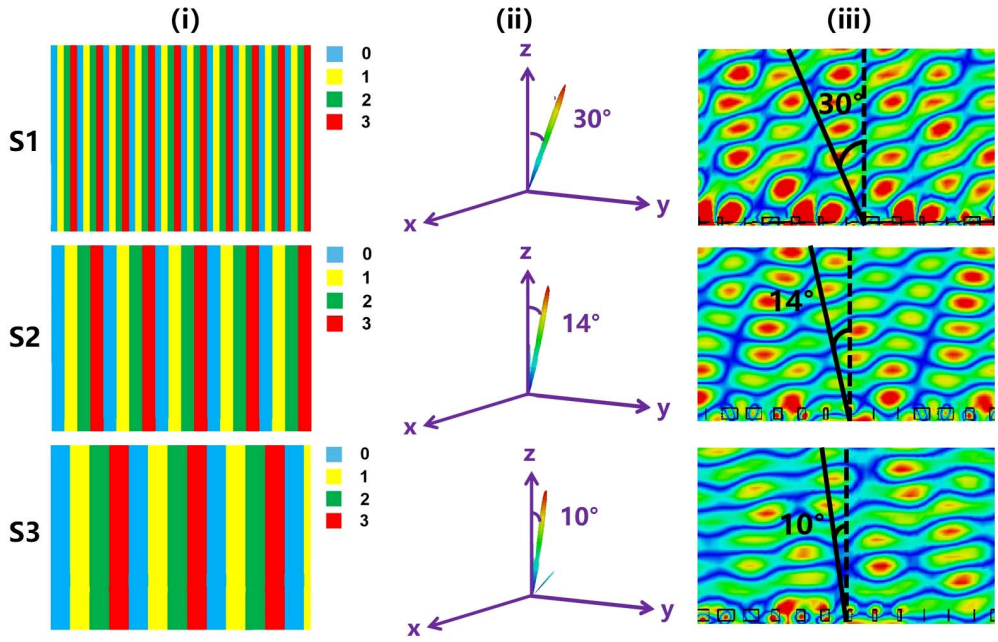

Fig. 3. Schematic diagram of the transmission-type basic sequence and simulation results. (i) S_1, S_2, S_3 sequence arrangement. (ii) Three-dimensional far-field scattering diagram. (iii) Near-field scattering diagram.

C. Non-Elementary Sequence Anomalous Transmission

Based on the far-field transmission angles of the three coded metasurface basic sequences obtained above, in order to realize the continuous control of the transmission angle, the coding design of the non-basic periodic sequence can be carried out according to the principle of coded grating addition. We know that, in the two-bit coding design, a new coding sequence can be obtained by performing four-bit operations on two known basic sequences [10].

The four-digit arithmetic rule is as follows: $0+0=0$, $0+1=1$, $1+1=2$, $1+2=3$, $2+2=0$, $2+3=1$, $3+3=2$, etc. The same rules of calculation apply to subtraction. For the convenience of description, a one-to-one correspondence is made between the coding sequence and the transmission angle. Through the above operations, the new sequence is $S_4 = 01302312\ldots$, $S_5 = 30011223\ldots$, $S_6 = 012012\ldots$, $S_7 = 301123\ldots$ (see Figs. 4–6). According to the four-bit operation of the above-mentioned new sequence and Eq. (6), there are

$$\theta_4 = \arcsin\left(\frac{\lambda}{4P} + \frac{\lambda}{8P}\right), \tag{7}$$

$$\theta_5 = \arcsin\left(\frac{\lambda}{4P} - \frac{\lambda}{8P}\right), \tag{8}$$

$$\theta_6 = \arcsin\left(\frac{\lambda}{4P} + \frac{\lambda}{12P}\right), \tag{9}$$

$$\theta_7 = \arcsin\left(\frac{\lambda}{4P} - \frac{\lambda}{12P}\right). \tag{10}$$

Given that $\lambda = 3000$ μm and $P = 1500$ μm, the theoretical values of the transmission angles of S_4, S_5, S_6, and S_7 sequences can be calculated, respectively, according to the above four formulas: $\theta_4 = 48.59°$, $\theta_5 = 14.47°$, $\theta_6 = 41.81°$, $\theta_7 = 19.47°$.

The newly obtained S_4, S_5, S_6, and S_7 coded supergratings are shown in Figs. 4–6. The simulation calculates that the transmission angles of the four non-basic sequences are $\theta_4 = 48°$, $\theta_5 = 14°$, $\theta_6 = 42°$, $\theta_7 = 19°$. It can be seen that the theoretical and simulation results are similar, which verifies the feasibility of the coded grating addition principle to continuously control the abnormal transmission angle.

On the basis of the above addition principle, we can perform four-bit operations on the non-basic sequence again to obtain a new coding sequence. For example, the new sequence is $S_8 = S_6 - S_7 = 333111\ldots$ (as shown in Fig. 7). It can be seen from the new sequence that the four-bit operation belongs to one-bit encoding, and the encoding period $\Gamma = 6P$. Although the encoding period Γ of the S_8 sequence is an integer multiple of P, the new sequence does not contain "0" and "2" unit elements, so the new sequence cannot be used as a basic sequence for four-bit operations. According to Eq. (6), it can be known that the transmission angle formula of the S_8 sequence is

$$\theta_8 = \arcsin\left(\frac{\lambda}{3P} - \frac{\lambda}{6P}\right). \tag{11}$$

Through theoretical calculation, the anomalous transmission angle of S_8 sequence is 19.47°. It can be seen from Fig. 7(b) that the S_8 sequence can obtain two mainlobes that are symmetrical about the z axis, and the mainlobes are equivalent to the energy being evenly distributed and emitted from different directions when passing through the super-coded grating. The reason why two mainlobes can be generated can be seen from the coding sequence. In the simulation, when the

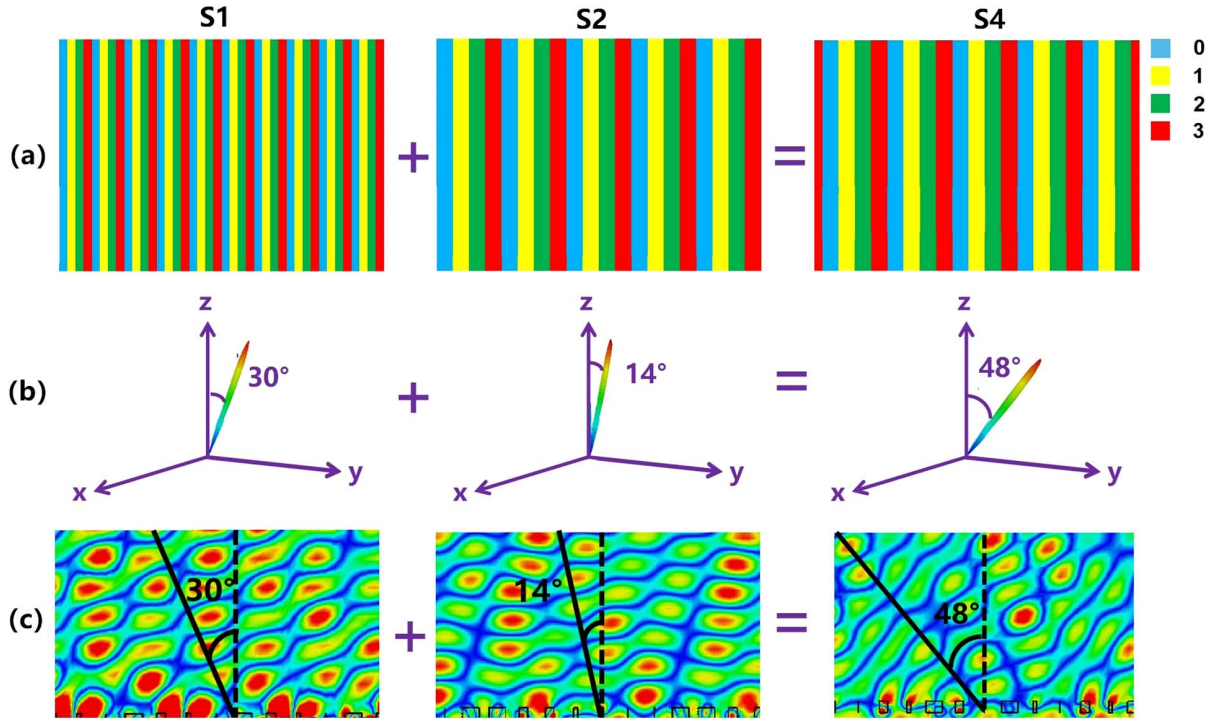

Fig. 4. Schematic diagram of S_4 metasurface and simulation results. (a) Coding sequence. (b) Three-dimensional far-field scattering. (c) Near-field scattering.

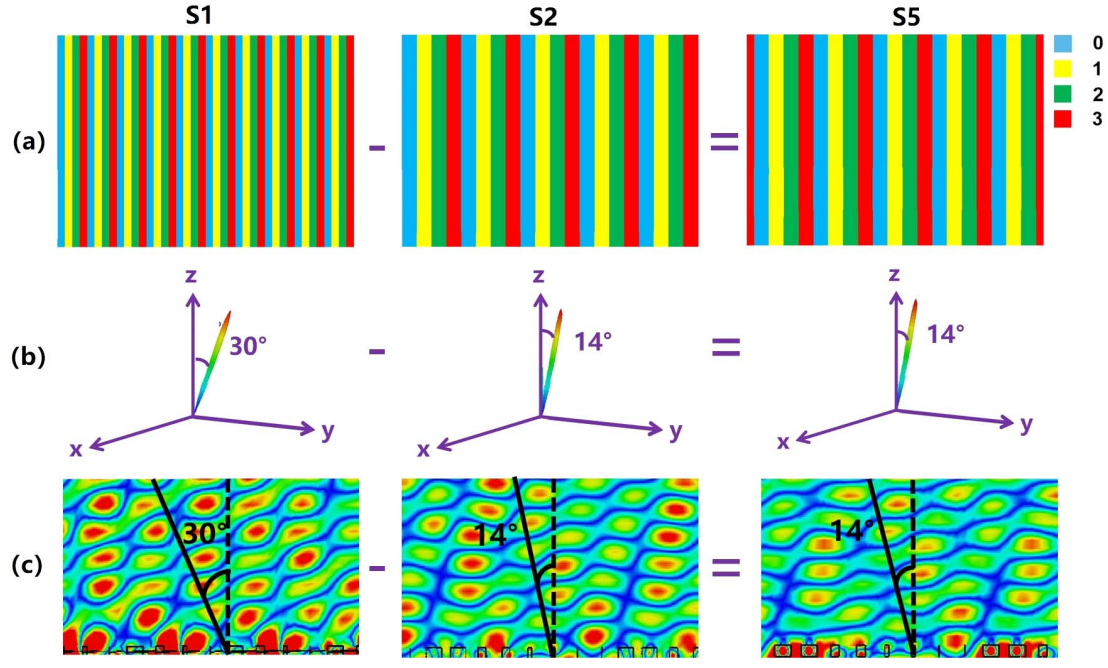

Fig. 5. Schematic diagram of S_5 metasurface and simulation results. (a) Coding sequence. (b) Three-dimensional far-field scattering. (c) Near-field scattering.

light source is set as a plane wave, the metasurfaces 333111… and 111333… are the same metasurface. The above-mentioned two phase gradients are just opposite, which in turn causes the mainlobe to be exactly symmetrical about the z axis.

The above are multiple sets of non-basic periodic sequences obtained by four-bit operations using two-bit coded numbers. The simulation and numerical calculations are in good agreement, indicating that the coded grating addition operation can

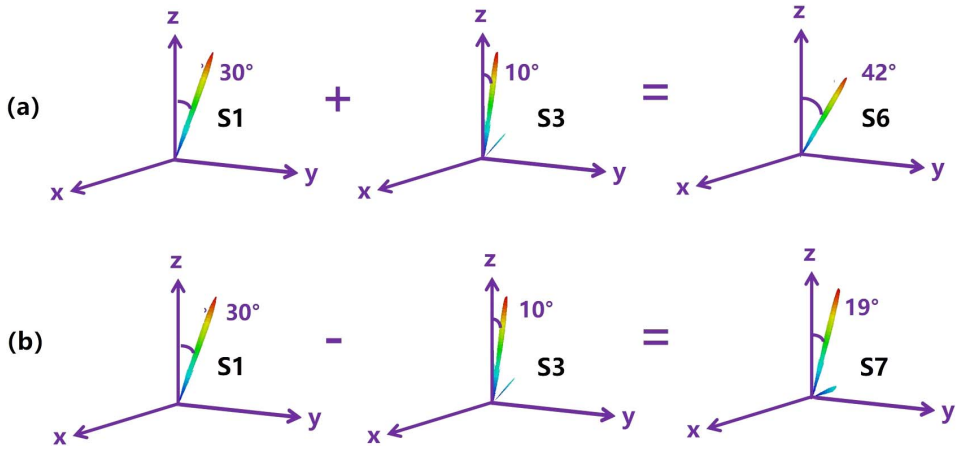

Fig. 6. Three-dimensional far-field scattering simulation results. (a) Three-dimensional far-field scattering diagram of S_6 sequence. (b) Three-dimensional far-field scattering diagram of S_7 sequence.

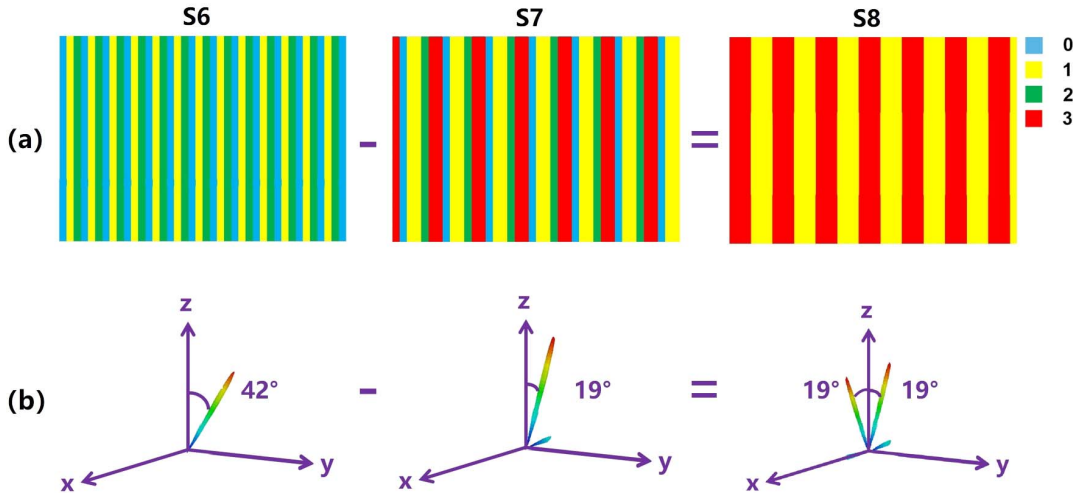

Fig. 7. Schematic diagram of S_8 metasurface and simulation results. (a) Coding sequence. (b) Three-dimensional far-field scattering.

continuously control the abnormal transmission angle. Obtaining aperiodic encoded sequences by four-bit operations is also applicable to one-bit encoded numbers. We calculate the basic sequences $S_{1'} = 0011\ldots$ and $S_{2'} = 00001111\ldots$ according to Eq. (6) to obtain a new coding sequence $S_{3'} = 11000011\ldots$, and the coding sequence is shown in Fig. 8.

The coding periods of coding sequences $S_{1'}$ and $S_{2'}$ are $\Gamma_{1'} = 4P = 6000\ \mu m$ and $\Gamma_{2'} = 8P = 12{,}000\ \mu m$, respectively. According to the generalized Snell's law formula $\theta = \arcsin(\lambda/\Gamma)$, the anomalous transmission angles $\theta_{1'} = 30°$ and $\theta_{2'} = 14.47°$ corresponding to the two basic sequences are, respectively, calculated. The simulation results can be seen from Fig. 8. The $S_{1'}$ sequence generates a symmetrical double beam with a transmission angle of 30°, and the $S_{2'}$ sequence generates a symmetrical double beam with a transmission angle of 15°. $S_{1'}$ sequence and $S_{2'}$ sequence are coded and subtracted to obtain a new sequence $S_{3'}$ with a coding period of 333,111…. According to Eq. (6), it can be calculated that the theoretical transmission angle of the $S_{3'}$ sequence is 14.47°, while the simulation result is 15°. The theoretical calculation and the simulation have a good consistency.

In addition to using the coded grating addition principle [59] to control the deflection angle of scattered beams, we also verified the cascaded metasurfaces to control the deflection of multiple beams, as shown in Fig. 9. The basic sequences $S_1 = 0123\ldots$ and $S_3 = 000111222333\ldots$ are physically superimposed in space to form a cascaded coded super grating $S_{4'}$. The cascaded grating can simultaneously generate two beams on a plane with deflection angles of 9° and 30°, respectively. These results verify that the substrate-free silicon grating structure [63] is also suitable for beam deflection with cascaded metasurfaces.

Two coded gratings are cascaded to realize the superposition of functions, which provides a new idea for the design of multifunctional devices. By superimposing different coded gratings, the performance of the system can be flexibly adjusted and optimized. For the aperiodic arrangement of the coded grating, it is inevitable to carry out a lot of operations when using the

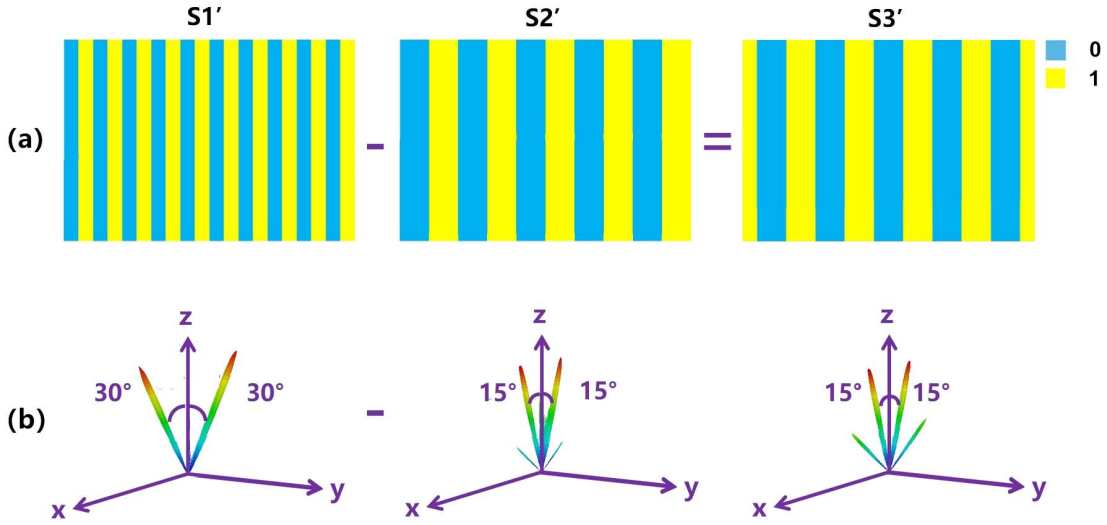

Fig. 8. Schematic diagram of $S_{3'}$ metasurface and simulation results. (a) Coding sequence. (b) Three-dimensional far-field scattering.

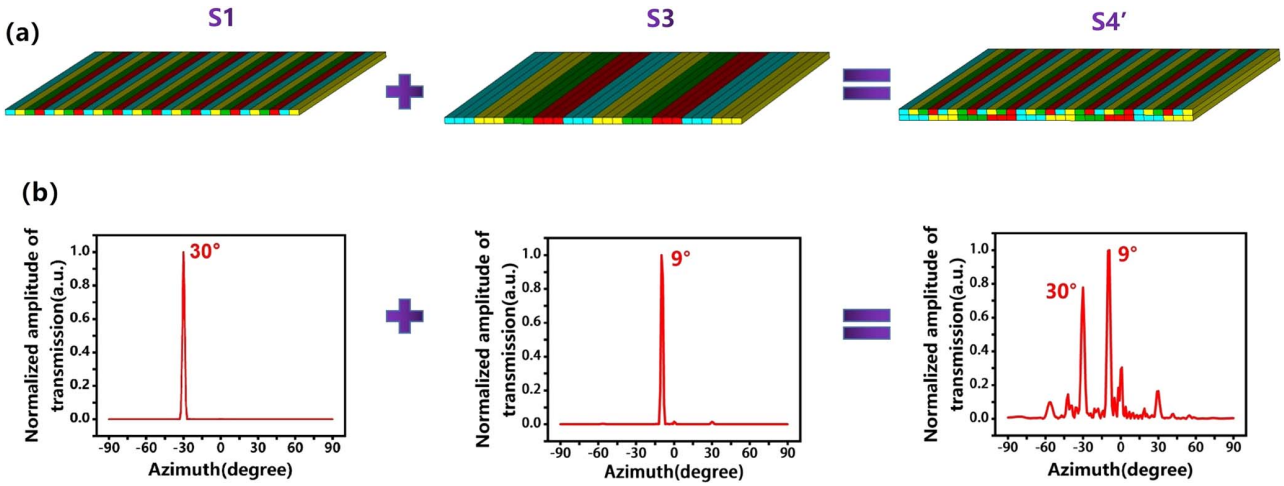

Fig. 9. Schematic diagram of cascaded metasurface and simulation results. (a) Coding sequence. (b) Two-dimensional scattering angle.

coding principle, and the coded grating is cascaded by the addition principle, which can reduce the cumbersome calculation and improve the design efficiency of multifunctional devices.

4. EXPERIMENTAL MEASUREMENTS AND RESULTS

In order to verify the designed array structure experimentally, we fabricated two simple substrate-free supergrating samples P_1 and P_2, and conducted data tests. The periods of the two unit samples are both 500 μm. For sample P_1, $\Gamma_1 = 4$ and $P = 2000$ μm; for sample P_2, $\Gamma_2 = 8$ and $P = 4000$ μm. In order to meet the requirements of the experiment, we selected double-throw high-resistance silicon with a crystal orientation of 110 [64,65] and a thickness of 300 μm for experimental verification. The experimental process is shown in Fig. 10.

We utilize classical photolithography techniques [66,67] to fabricate substrate-free coded grating samples. First, a layer of SiO_2 is oxidized on the entire surface of the silicon wafer, as shown in Fig. 10(b). The oxidized silicon wafer was cut according to the size of the mask [68], and the silicon wafer used in the experiment was thoroughly cleaned (cleaned with acetone and water) and then dried on a dryer for 10 min. We put the cleaned silicon wafer on the glue leveling table, coat a layer of tackifier and photoresist [69] on the silicon wafer in turn [as shown in Fig. 10(c)], and dry it for 5 min after coating and 1.5 min. As shown in Fig. 10(d), we align the silicon wafer with the mask and place it under a mercury lamp for exposure for 11 s. After the exposure, the silicon wafer is placed in the developer [70] (0.9 g NaOH + 100 mL H_2O) for 8 s [Fig. 10(e)], and then the silicon wafer is quickly rinsed under flowing plasma water. As shown in Fig. 10(f), after the development, the silicon wafer is dried for 1.5 min, and then the silicon

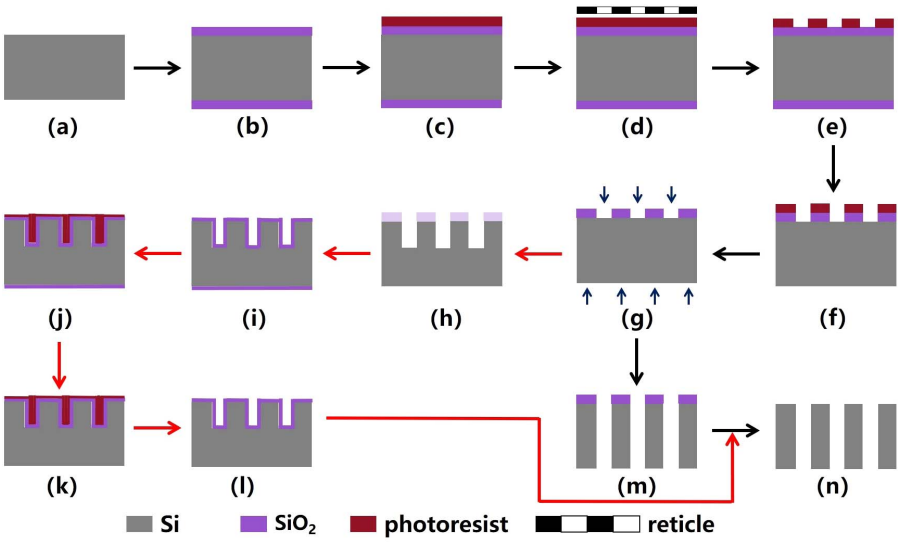

Fig. 10. Schematic diagram of the experimental process.

wafer is placed in a cleaning solution ($HF:NH_4F:H_2O = 3:6:10$) for 10–12 min to wash off the bottom SiO_2. We use the method of wet etching [71] to etch in the etching solution (20 mL C_4HNO + 6 mL C_3H_8O) for 4.5–5 h [wet etching is shown in Fig. 10(g); we put the silicon wafer in the etching solution, and the upper and lower layers will be etched at the same time] and get the experimental sample with SiO_2 on the top layer [72]. Finally, the designed experimental structure can be obtained by washing off the SiO_2 on the top layer. Since the etching time is too long, the SiO_2 on the surface of the structure will be destroyed, resulting in uneven adhesion of SiO_2 on the surface [73]. For the accuracy of the experiment, all the SiO_2 on the silicon surface was washed off first, and then a layer of SiO_2 was re-oxidized, so that a uniform layer of SiO_2 was attached to the entire surface of the silicon wafer as shown in Fig. 10(i). After the oxidation is completed, a layer of photoresist [69] is evenly coated on the top layer of the grating bars [as shown in Fig. 10(j)] to prevent damage to the top silicon structure during the subsequent wet etching process. Finally, the bottom SiO_2 and Si are, respectively, etched away to obtain the designed substrate-free silicon grating.

As shown in Fig. 11, through the above experimental process, we produced two coded samples P_1 and P_2, both of which consisted of 40 × 30 unit particles. Due to the limitation of experimental conditions and the inhomogeneity of wet etching, the thicknesses of the final grating samples P_1 and P_2 were 135 μm and 124 μm, respectively. The bar widths were 292 μm and 129 μm, respectively.

We built a tunable continuous terahertz wave system [74], and the test platform is shown in Fig. 12. First, we fix the

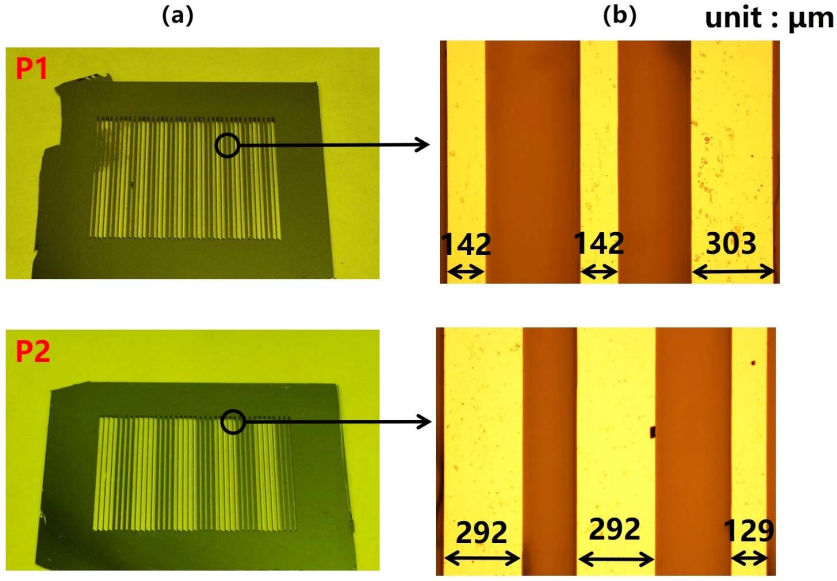

Fig. 11. Schematic diagram of experimental samples P_1 and P_2. (a) Sample picture. (b) 10 times microscope magnified picture.

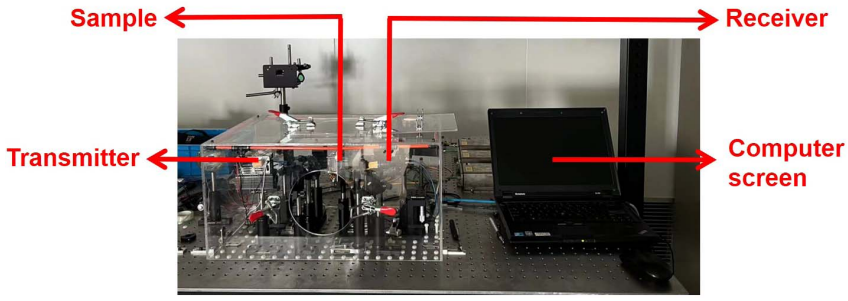

Fig. 12. Experimental test platform.

experimental sample on the support frame and adjust the height of the support frame so that the incident light, the sample, and the receiving end are on the same horizontal plane. Based on the principle of photon mixing [75–77], two independent semiconductor lasers are used as the irradiation light source of the butterfly photoconductive antenna [78]. The incident light frequency ranges from 0.05 THz to 1 THz, and the computer is connected to the receiving end to display the test data. We set the parameters of the software before the experimental test, and we set the lowest frequency point to 0.05 THz and the highest frequency point to 0.5 THz. We tested the transmittance of samples P_1 and P_2 in the range of 0.05 THz to 0.4 THz, and the test results are shown in Fig. 13.

It can be clearly seen from the figure that the transmittance of sample P_1 at 0.1 THz is about 70%, the transmittance of sample P_2 is about 69%, and the transmittance of cascaded metasurface is about 52%. The reasons for the deviation between the experimental data and the simulated data may be as follows: on the one hand, there may be preparation errors in the process of metasurface preparation, especially in the process of wet corrosion, when the width of the prepared grating strips and simulation errors will occur. In addition, because the wet corrosion method is to immerse the sample in the corrosive liquid for corrosion, a large number of bubbles will be generated during the corrosion process, and the sample will float on the surface of the corrosive liquid, resulting in different corrosion rates on the

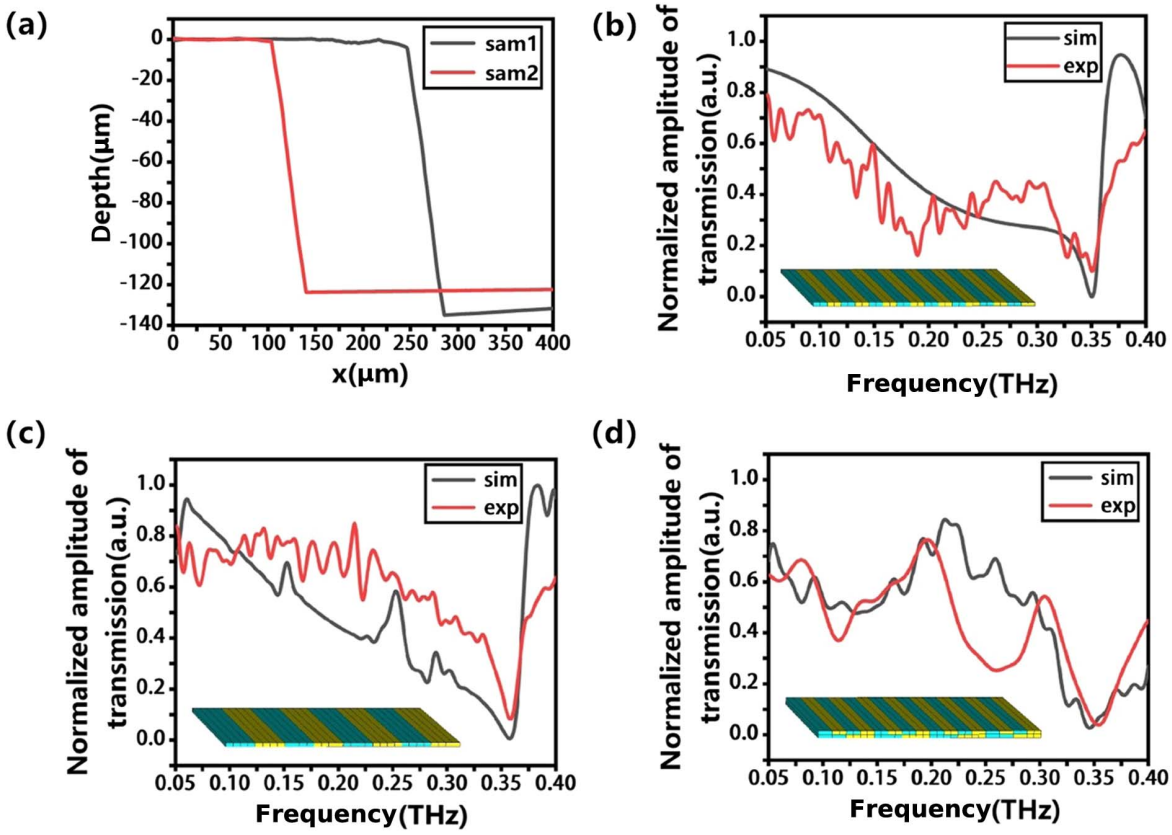

Fig. 13. Comparison between simulation and experiment of samples P_1 and P_2. (a) Schematic diagram of test thickness of samples P_1 and P_2. (b) Comparison of simulated and experimental transmittance of P_1. (c) Comparison diagram of P_2 transmittance simulation and experiment. (d) Comparison of simulated and experimental transmittance of cascade metasurface.

upper and lower surfaces, and eventually the thickness of the prepared sample is inconsistent. In addition, the substrate-free silicon grating structure is prepared, and the side of the grating strip may be corroded during the wet corrosion process, resulting in changes in the actual width of the grating strip and resulting in errors. On the other hand, because the designed structure is a baseless grating metasurface, the step meter cannot accurately measure the width and depth of the small grating gap during the test process, resulting in a gap between the actual measurement results and the theoretical results. Although there are errors in the test and simulation data, the overall trend of the transmission efficiency curve is consistent within the range of 0.05–0.4 THz. The highly efficient transmission properties of P_1 and P_2 can also be indirectly verified at 0.1 THz.

Laboratory tests use TeraSense's terahertz source as well as terahertz imaging cameras. The terahertz camera bandwidth range is 0.05 THz to 0.7 THz, the high-speed image acquisition rate can reach up to 50 frames per second, and the number of pixels is 32 × 32. The experimental platform is shown in Fig. 14(a) and consists of an antenna speaker, lens, terahertz camera, display, etc. A light source with a frequency of 0.1 THz is emitted through an antenna horn, and the outgoing beam diverges outward in a scattered manner. After passing through the first lens, the beam is converted into a parallel beam, and then the second lens is used to converge the parallel light. The incident beam is concentrated on the metasurface, and after passing through the metasurface, it is received by a terahertz camera. The application is designed by LabView to receive and process data on the computer side. The experimental test results are shown in Fig. 14(b), and we can see that there is a gap between the simulation effect of the prepared coding array at 0.1 THz and the experimental results. In region (ii) of Figure 14, we select four points with obvious scattering effects, and by comparing the two-dimensional far-field scattering patterns of samples P_1, P_2, and cascaded metasurfaces, we find that the superposition of the cascade metasurface function is in line, thereby indirectly verifying the feasibility of cascade metasurface manipulation beam.

5. CONCLUSION

We propose a coding supergrating structure, and the coding units are all made of substrate-free silicon material. The parameters of the unit structure are optimized so that the unit particles have a complete 2π transmission phase coverage under the condition of 0.1 THz and co-polarization, and there is a phase

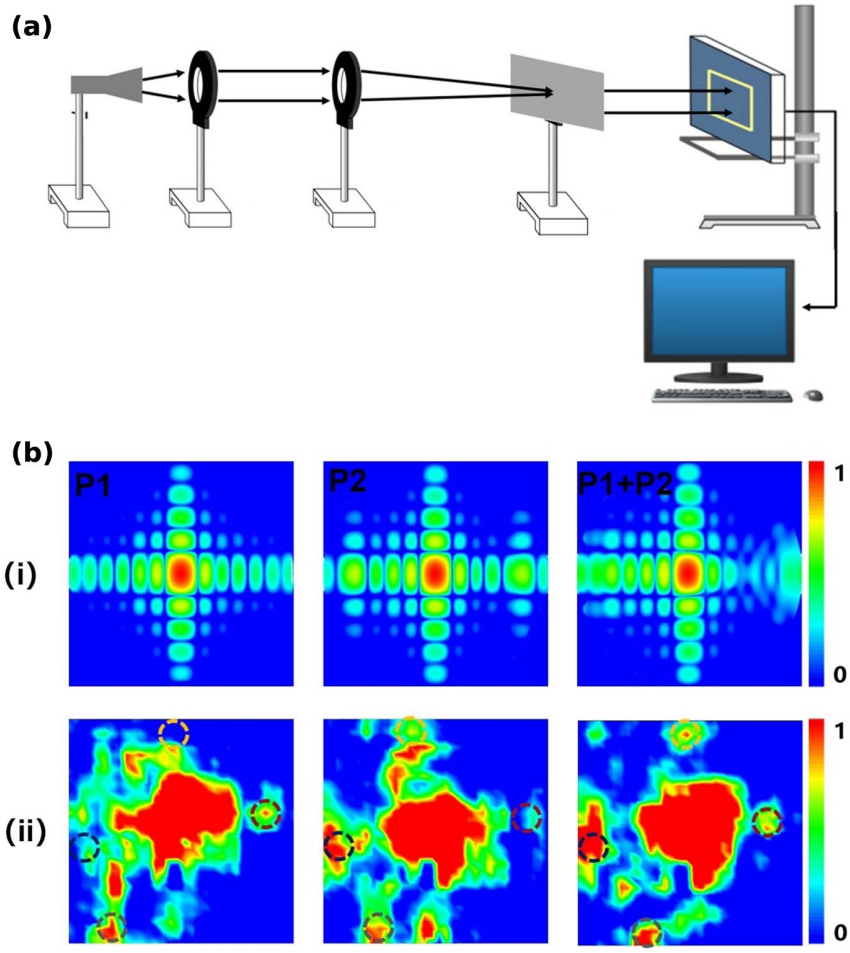

Fig. 14. Experimental diagram. (a) Experimental platform. (b) Far-field scattering pattern. (i) Samples P_1, P_2, and cascaded metasurface simulation patterns. (ii) Samples P_1, P_2, and cascaded metasurface test results.

difference of $\pi/2$ between each unit particle. We design multiple sets of simple basic sequences and solve the theoretical far-field scattering beam elevation angle through the generalized Snell theorem. For the far-field scattered beam angles of other non-basic sequences, the corresponding transmission angle can be obtained by redetermining the encoding period Γ through the four-bit operation of the basic sequence. We obtained coded supergratings with high transmittance and large deflection angle. We verified the control of the cascaded metasurface on the deflection angle of the incident light, and the theoretical values obtained are basically consistent with the simulation results. We demonstrate the feasibility of the encoded grating addition principle to continuously control the far-field scattering angle on a substrate-free all-dielectric encoded supergrating.

Funding. Natural Science Foundation of Zhejiang Province (LZ21A040003, LY22F050001); National Natural Science Foundation of China (62175224).

Disclosures. The authors declare no conflicts of interest.

Data Availability. Data underlying the results presented in this paper are not publicly available at this time but may be obtained from the authors upon reasonable request.

REFERENCES

1. X. He, "Tunable terahertz graphene metamaterials," Carbon **82**, 229–237 (2015).
2. X. He, X. Zhong, F. T. Lin, and W. Z. Shi, "Investigation of graphene assisted tunable terahertz metamaterials absorber," Opt. Mater. Express **6**, 331–342 (2016).
3. H. J. Dai, Y. J. Zhao, and C. Yu, "A multi-elements chessboard random coded metasurface structure for ultra-wideband radar cross section reduction," IEEE Access **8**, 56462–56468 (2020).
4. X. Y. He, F. Liu, F. T. Lin, and W. Z. Shi, "Tunable 3D Dirac-semimetals supported mid-IR hybrid plasmonic waveguides," Opt. Lett. **46**, 472–475 (2021).
5. X. Y. He, F. Liu, F. T. Lin, and W. Z. Shi, "Tunable terahertz Dirac semimetal metamaterials," J. Phys. D **54**, 235103 (2021).
6. J. Peng, X. Y. He, C. Y. Y. Shi, J. Leng, F. T. Lin, F. Liu, H. Zhang, and W. Z. Shi, "Investigation of graphene supported terahertz elliptical metamaterials," Phys. E **124**, 114309 (2020).
7. Y. Peng, C. J. Shi, Y. M. Zhu, M. Gu, and S. L. Zhuang, "Terahertz spectroscopy in biomedical field: a review on signal-to-noise ratio improvement," PhotoniX **1**, 12 (2020).
8. C. J. Shi, X. Wu, and Y. Peng, "Applications of terahertz imaging technology in tumor detection," Opto-Electron. Eng. **47**, 190638 (2020).
9. W. W. Wan, J. Gao, and X. Y. Yang, "Metasurface holograms for holographic imaging," Adv. Opt. Mater. **5**, 1700541 (2017).
10. H. Wang, L. X. Liu, C. D. Zhou, J. L. Xu, M. N. Zhang, S. Y. Teng, and Y. J. Cai, "Vortex beam generation with variable topological charge based on a spiral slit," Nanophotonics **8**, 317–324 (2019).
11. C. L. Xu, B. K. Wang, Y. Q. Pang, J. F. Wang, M. B. Yan, W. J. Wang, A. X. Wang, J. M. Jiang, and S. B. Qu, "Hybrid metasurfaces for infrared-multiband radar stealth-compatible materials applications," IEEE Access **7**, 147586–147595 (2019).
12. P. C. Huo, M. W. Song, W. Q. Zhu, C. Zhang, L. Chen, H. J. Lezec, Y. Q. Lu, A. Agrawal, and T. Xu, "Photorealistic full-color nanopainting enabled by a low-loss metasurface," Optica **7**, 1171–1172 (2020).
13. J. X. Cai, F. Zhang, M. B. Pu, Y. Chen, Y. H. Guo, T. Xie, X. D. Feng, X. L. Ma, X. Li, H. L. Yu, and X. G. Luo, "All-metallic high-efficiency generalized Pancharatnam–Berry phase metasurface with chiral meta-atoms," Nanophotonics **11**, 1961–1968 (2022).
14. X. F. Jing, Y. N. Xu, H. Y. Gan, Y. W. He, and Z. Hong, "High refractive index metamaterials by using higher order modes resonances of hollow cylindrical nanostructure in visible region," IEEE Access **7**, 144945–144956 (2019).
15. L. Jiang, B. Fang, Z. G. Yan, J. Fan, C. K. Qi, J. J. Liu, Y. W. He, C. X. Li, X. F. Jing, H. X. Gan, and Z. Hong, "Terahertz high and near-zero refractive index metamaterials by double layer metal ring microstructure," Opt. Laser Technol. **123**, 105949 (2020).
16. B. Fang, Z. Y. Cai, Y. D. Peng, C. X. Li, Z. Hong, and X. F. Jing, "Realization of ultrahigh refractive index in terahertz region by multiple layers coupled metal ring metamaterials," J. Electromagn. Waves Appl. **33**, 1375–1390 (2019).
17. A. Vaskin, S. Liu, S. Addamane, P. P. Vabishchevich, Y. M. Yang, G. Balarishnan, M. B. Sinclair, T. Pertsch, I. Brener, and I. Staude, "Manipulation of quantum dot emission with semiconductor metasurfaces exhibiting magnetic quadrupole resonances," Opt. Express **29**, 5567–5579 (2021).
18. X. F. Jing, S. Z. Jin, Y. Tian, P. Liang, Q. M. Dong, and L. Wang, "Analysis of the sinusoidal nanopatterning grating structure," Opt. Laser Technol. **48**, 160–166 (2013).
19. Y. Fu, X. J. Fu, L. Shi, and T. J. Cui, "Grating-like terahertz metasurface for large-deflection-angle beam manipulations," Appl. Sci. **12**, 12322 (2022).
20. M. R. Akram, G. W. Ding, K. Chen, Y. J. Feng, and W. R. Zhu, "Ultra-thin single layer metasurfaces with ultra-wideband operation for both transmission and reflection," Adv. Mater. **32**, 1907308 (2020).
21. W. M. Wang, X. F. Jing, J. Y. Zhao, Y. Y. Li, and Y. Tian, "Improvement of accuracy of simple methods for design and analysis of a blazed phase grating microstructure," Opt. Appl. **47**, 183–198 (2017).
22. C. Y. Jin, W. Wu, L. Gao, B. F. Gao, J. X. Chen, W. Cai, M. X. Ren, and J. J. Xu, "Fabrication of lithium niobate metasurfaces via a combination of FIB and ICP-RIE," Chin. Opt. Lett. **20**, 113602 (2022).
23. J. Leng, J. Peng, A. Jin, D. Cao, D. J. Liu, X. Y. He, F. T. Lin, and F. Liu, "Investigation of terahertz high *Q*-factor of all-dielectric metamaterials," Opt. Laser Technol. **146**, 107570 (2022).
24. X. H. Xie, Y. P. Deng, and S. L. Johnson, "Compact and robust supercontinuum generation and post-compression using multiple thin plates," High Power Laser Sci. Eng. **9**, e66 (2021).
25. J. G. Wang, Z. K. Shao, Y. H. Wen, X. D. Qiu, Y. J. Chen, Y. F. Zhang, S. Y. Yu, and L. X. Chen, "All-dielectric metasurface grating for on-chip multi-channel orbital angular momentum generation and detection," Opt. Express **27**, 18794–18802 (2019).
26. P. F. Wang, "Ultra-high-*Q* resonances in terahertz all-silicon metasurfaces based on bound states in the continuum," Photon. Res. **10**, 2743–2750 (2022).
27. V. Shanmugan, F. Y. He, J. J. Liu, F. Z. Shu, B. Fang, T. T. Lang, X. F. Jing, and Z. Hong, "Dielectric-based distributed Bragg reflector (DBR) mirrors for tunable MOEMS applications," Proc. SPIE **5641**, 7–18 (2004).
28. M. R. Akram, M. Q. Mehmood, X. D. Bai, R. H. Jin, M. Premaratne, and W. R. Zhu, "High efficiency ultra-thin transmissive metasurfaces," Adv. Opt. Mater. **7**, 1801628 (2019).
29. H. X. Xu, G. W. Hu, L. Han, M. H. Jiang, Y. J. Huang, Y. Li, X. M. Yang, X. H. Ling, L. Z. Chen, J. L. Zhao, and C. W. Qiu, "Chirality-assisted high-efficiency metasurfaces with independent control of phase, amplitude, and polarization," Adv. Opt. Mater. **7**, 1801479 (2019).
30. X. D. Bai, F. W. Kong, Y. T. Sun, G. F. Wang, J. Y. Qian, X. B. Li, A. J. Cao, C. He, L. Liang, R. H. Jin, and W. R. Zhu, "High-efficiency transmissive programable metasurface for multi-mode OAM generations," Adv. Opt. Mater. **8**, 2000570 (2020).
31. M. R. Akram, X. D. Bai, R. H. Jin, G. A. E. Vandenbosch, M. Premaratne, and W. R. Zhu, "Photon spin Hall effect based ultra-thin transmissive metasurface for efficient generation of OAM waves," IEEE Trans. Antennas Propag. **67**, 4650–4658 (2019).
32. H. X. Xu, G. W. Hu, M. H. Jiang, S. W. Tang, Y. Z. Wang, C. H. Wang, Y. J. Huang, X. H. Liang, H. W. Liu, and J. F. Zhou, "Wavevector and frequency multiplexing performed by a spin-decoupled multichannel metasurface," Adv. Mater. Technol. **5**, 1900710 (2020).
33. P. Pottier and M. Packirisamy, "Mono-order high-efficiency dielectric concave diffraction grating," J. Lightwave Technol. **30**, 2922–2928 (2012).
34. H. X. Xu, G. W. Hu, Y. Li, L. Han, J. L. Zhao, Y. M. Sun, F. Yuan, G. M. Wang, Z. H. Jiang, X. H. Ling, and T. J. Cui, "Interference-assisted

kaleidoscopic meta-plexer for arbitrary spin-wavefront manipulation," Light Sci. Appl. **8**, 3 (2019).
35. J. T. Li, J. Li, C. L. Zheng, S. L. Wang, M. Y. Li, H. L. Zhao, J. H. Li, Y. T. Zhang, and J. Q. Yao, "Dynamic control of reflective chiral terahertz metasurface with a new application developing in full grayscale near field imaging," Carbon **172**, 189–199 (2021).
36. J. T. Li, G. C. Wang, Z. Yue, J. Y. Liu, J. Li, C. L. Zheng, Y. T. Zhang, Y. Zhang, and J. Q. Yao, "Dynamic phase assembled terahertz metalens for reversible conversion between linear polarization and arbitrary circular polarization," Opto-Electron. Adv. **5**, 210062 (2022).
37. H. R. Lv, X. Q. Lu, Y. S. Han, Z. Mou, C. D. Zhou, S. Y. Wang, and S. Y. Teng, "Metasurface cylindrical vector light generators based on nanometer holes," New J. Phys. **21**, 123047 (2019).
38. H. R. Lv, X. Q. Lu, Y. S. Han, Z. Mou, and S. Y. Teng, "Multifocal metalens with a controllable intensity ratio," Opt. Lett. **44**, 2518–2521 (2019).
39. H. X. Xu, Y. Z. Wang, C. H. Wang, M. Z. Wang, S. J. Wang, F. Ding, Y. J. Huang, X. K. Zhang, H. W. Liu, X. H. Ling, and W. Huang, "Deterministic approach to achieve full-polarization cloak," Research **001**, 6382172 (2021).
40. T. Ebert, R. Heber, T. Abel, J. Bieker, G. Schaumann, and M. Roth, "Targets with cone-shaped microstructures from various materials for enhanced high-intensity laser–matter interaction," High Power Laser Sci. Eng. **9**, 02000e24 (2021).
41. L. Carletti, M. Gandolfi, D. Rocco, A. Tognazzi, D. C. Ceglia, M. A. Vincenti, and D. C. Angelis, "Reconfigurable nonlinear response of dielectric and semiconductor metasurfaces," Nanophotonics **10**, 4209–4221 (2021).
42. J. P. Li, R. H. Jin, J. P. Geng, X. L. Liang, K. Wang, M. Premaratne, and W. R. Zhu, "Design of a broadband metasurface Luneburg lens for full-angle operation," IEEE Trans. Anntenas Propag. **67**, 2442–2451 (2019).
43. J. Zhang, H. Zhang, W. X. Yang, K. Chen, X. Z. Wei, Y. J. Feng, R. H. Jin, and W. R. Zhu, "Dynamic scattering steering with graphene-based coding meta-mirror," Adv. Opt. Mater. **8**, 2000683 (2020).
44. B. Fang, B. Y. Li, Y. D. Peng, C. X. Li, Z. Hong, and X. F. Jing, "Polarization-independent multiband metamaterials absorber by fundamental cavity mode of multilayer microstructure," Microw. Opt. Technol. Lett. **61**, 2385–2391 (2019).
45. X. F. Jing, X. C. Gui, P. W. Zhou, and Z. Hong, "Physical explanation of Fabry-Pérot cavity for broadband bilayer metamaterials polarization converter," J. Lightwave Technol. **36**, 2322–2327 (2018).
46. Z. Y. Liu, L. M. Qi, F. Lan, C. W. Lan, J. Yang, and X. Tao, "A VO_2 film-based multifunctional metasurface in the terahertz band," Chin. Opt. Lett. **20**, 013602 (2022).
47. L. Jiang, Z. Yu, W. Zhao, Z. Yang, Y. Peng, Y. Zhou, X. Lin, and S. Jin, "Self-assembled MXene-Au multifunctional nanomaterials with various shapes for label-free SERS detection of pathogenic bacteria and photothermal sterilization," Anal. Chem. **95**, 1721–1730 (2023).
48. Y. Tian, X. F. Jing, H. Y. Gan, C. X. Li, and Z. Hong, "Free control of far-field scattering angle of transmission terahertz wave using multilayer split-ring resonators' metasurfaces," Front. Phys. **15**, 62502 (2020).
49. Z. Yu, L. Jiang, R. Liu, W. Zhao, Z. Yang, J. Zang, and S. Jin, "Versatile self-assembled MXene-Au nanocomposites for SERS detection of bacteria, antibacterial and photothermal sterilization," Chem. Eng. J. **426**, 131914 (2021).
50. Y. Zhu, B. B. Lu, Z. Y. Fan, F. Y. Yue, X. F. Zang, A. V. Balakin, A. P. Shkurinov, Y. M. Zhu, and S. L. Zhuang, "Geometric metasurface for polarization synthesis and multidimensional multiplexing of terahertz converged vortices," Photon. Res. **10**, 1517–1532 (2022).
51. L. D. Shao, J. Zhang, R. Ivan, and W. R. Zhu, "Electrically reconfigurable microwave metasurfaces," Chin. Opt. Lett. **20**, 103601 (2022).
52. J. T. Li, J. Li, C. L. Zheng, Z. Yue, S. L. Wang, M. Y. Li, H. L. Zhao, Y. L. Zhang, and J. Q. Yao, "Free switch between bound states in the continuum (BIC) and quasi-BIC supported by graphene-metal terahertz metasurfaces," Carbon **182**, 506–515 (2021).
53. X. Q. Lu, X. Y. Zeng, H. R. Lv, Y. S. Han, Z. Mou, C. X. Liu, S. Y. Wang, and S. Y. Teng, "Polarization controllable plasmonic focusing based on nanometer holes," Nanotechnology **31**, 135201 (2020).
54. X. Y. He, F. Liu, F. T. Lin, and W. Z. Shi, "3D Dirac semimetal supported tunable TE modes," Ann. Phys. **534**, 2100355 (2022).
55. C. H. Wang, X. X. He, Y. Z. Wang, C. Zhang, S. J. Wang, M. Z. Wang, and X. Yang, "Heterogeneous amplitude-phase metasurface for distinct wavefront manipulation," Adv. Photon. Res. **2**, 2100102 (2021).
56. S. Y. Teng, Q. Zhang, H. Wang, L. X. Liu, and H. R. Lv, "Conversion between polarization states based on metasurface," Photon. Res. **7**, 246–250 (2019).
57. J. T. Li, J. Li, C. L. Zheng, Z. Yue, D. Y. Yang, S. L. Wang, M. Y. Li, Y. T. Zhang, and J. Q. Yao, "Spectral amplitude modulation and dynamic near-field displaying of all-silicon terahertz metasurfaces supporting bound states in the continuum," Appl. Phys. Lett. **119**, 241105 (2021).
58. J. Zhang, X. Z. Wei, I. D. Rukhlenko, H. T. Chen, and W. R. Zhu, "Electrically tunable metasurface with independent frequency and amplitude modulations," ACS Photon. **7**, 265–271 (2020).
59. S. S. Cai, W. H. Hu, Y. M. Liu, J. Ning, S. X. Feng, C. Jin, L. L. Huang, and X. Li, "Optical fiber hydrogen sensor using metasurfaces composed of palladium," Chin. Opt. Lett. **20**, 053601 (2022).
60. J. Y. Zhao, X. F. Jing, W. M. Wang, Y. Tian, D. S. Zhu, and G. H. Shi, "Steady method to retrieve effective electromagnetic parameters of bianisotropic metamaterials at one incident direction in the terahertz region," Opt. Laser Technol. **95**, 56–62 (2017).
61. H. X. Xu, C. H. Wang, Y. Z. Wang, M. Z. Wang, S. J. Wang, G. W. Hu, S. W. Tang, Y. J. Huang, X. H. Ling, W. Huang, and C. W. Qiu, "Spin-encoded wavelength-space multitasking Janus metasurfaces," Adv. Opt. Mater. **9**, 2100190 (2021).
62. B. Fang, D. T. Feng, P. Chen, L. J. Shi, J. H. Cai, J. M. Li, C. X. Li, Z. Hong, and X. F. Jing, "Broadband cross-circular polarization carpet cloaking based on a phase change material metasurface in the mid-infrared region," Front. Phys. **17**, 53502 (2022).
63. J. T. Li, J. Li, C. L. Zheng, Z. Yue, S. L. Wang, M. Y. Li, H. L. Zhao, Y. T. Zhang, and J. Q. Yao, "Active controllable spin-selective terahertz asymmetric transmission based on all-silicon metasurfaces," Appl. Phys. Lett. **118**, 221110 (2021).
64. L. Jiang, B. Fang, Z. G. Yan, C. X. Li, J. P. Fu, H. Y. Gan, Z. Hong, and X. F. Jing, "Improvement of unidirectional scattering characteristics based on multiple nanospheres array," Microw. Opt. Technol. Lett. **62**, 2405–2414 (2020).
65. A. Z. Khachatrian, A. S. Avanesyan, V. N. Aghabekyan, and A. F. Parsamyan, "The Fresnel picture of scattering of a plane wave on a diffraction grating," J. Contemp. Phys. **57**, 243–253 (2022).
66. H. S. Kim, J. M. Kim, Y. S. Bang, E. S. Song, C. H. Ji, and Y. K. Kim, "Fabrication of a vertical sidewall using double-sided anisotropic etching of <100> oriented silico," J. Micromech. Microeng. **22**, 095014 (2012).
67. M. Nagai, Y. Nakamura, T. Yamada, T. Tabakoya, T. Matsumoto, T. Inokuma, C. E. Nebel, T. Makino, S. Yamasaki, and N. Tokuda, "Formation of U-shaped diamond trenches with vertical {111} sidewalls by anisotropic etching of diamond (110) surfaces," Diam. Relat. Mater. **103**, 107713 (2020).
68. Y. C. Zheng, K. Q. Qiu, X. L. Jiang, Q. B. Wang, L. X. Wu, L. L. Bi, Y. L. Hong, E. M. Campo, E. A. Dobisz, and L. A. Eldada, "Fabrication of high aspect ratio silicon gratings by interference lithography and potassium hydroxide anisotropic etch technique," Proc. SPIE **9170**, 917018 (2014).
69. M. Ahn, R. K. Heilmann, and M. L. Schattenburg, "Fabrication of ultra-high aspect ratio freestanding gratings on silicon-on-insulator wafers," J. Vac. Sci. Technol. B **25**, 2593–2597 (2007).
70. S. Q. Qian, Y. Y. Wu, K. Bao, Y. D. Zhou, H. B. Cao, and H. Zhang, "Experimental study of metal bipolar plate microchannels fabrication using the through mask electrochemical machining," Int. J. Electrochem. Sci. **14**, 9273–9282 (2019).
71. Sutikno, Susilo, and H. D. Raharja, "Photoresist: fabrication, characterization and its sensitivity on the exposures of x-ray and ultraviolet," IOP Conf. Ser. Mater. Sci. Eng. **367**, 012022 (2018).
72. J. J. Santillan, M. Harumoto, T. Motono, A. F. D. Santos, C. Mori, Y. J. Tanaka, H. Stokes, M. Asai, and T. Itani, "Alternative developer solution process for EUV lithography: ethyltrimethylammonium hydroxide (ETMAH)," Proc. SPIE **11609**, 116090W (2021).

73. C. C. Chiang, X. Xia, J. S. Li, F. Ren, and S. J. Pearton, "Selective wet and dry etching of NiO over β-Ga_2O_3," ECS J. Solid State Sci. Technol. **11**, 104001 (2022).
74. R. Xia, X. F. Jing, X. C. Gui, Y. Tian, and Z. Hong, "Broadband terahertz half-wave plate based on anisotropic polarization conversion metamaterials," Opt. Mater. Express **7**, 977–988 (2017).
75. S. K. Behera, S. Suri, N. P. Salowitz, M. Nosonovsky, and P. K. Rohatgi, "The effect of surface roughness and composition on wetting and corrosion of Al-Si alloys," Israel J. Chem. **60**, 577–585 (2020).
76. B. Gai, J. B. Liu, P. Y. Wang, Y. Chen, S. Hu, and J. W. Guo, "Terahertz emitting and four wave mixing details in $6P_{3/2}\rightarrow 11D_J$ pumped cesium vapor," J. Quant. Spectrosc. Radiat. Transfer **258**, 107351 (2021).
77. H. X. Xu, Y. H. Wang, C. H. Wang, M. Z. Wang, S. J. Wang, F. Ding, Y. J. Huang, X. K. Zhang, H. W. Liu, X. H. Ling, and W. Huang, "Deterministic approach to achieve full-polarization cloak," Research **2021**, 6382172 (2021).
78. R. Liu, L. Jiang, Z. Yu, X. Jing, X. Liang, D. Wang, B. Yang, C. Lu, W. Zhou, and S. Jin, "MXene ($Ti_3C_2T_x$)-Ag nanocomplex as efficient and quantitative SERS biosensor platform by *in-situ* PDDA electrostatic self-assembly synthesis strategy," Sens. Actuators B **333**, 129581 (2021).